Implementation of Premixed Equilibrium Chemistry Capability in OVERFLOW

M. E. Olsen *
NASA Ames Research Center Moffett Field, CA 94035

Y. Liu †
NASA Ames Research Center Moffett Field, CA 94035

M. Vinokur ‡
ELORET Corp. Sunnyvale , CA 94087

T. Olsen §
ELORET Corp. Sunnyvale , CA 94087

An implementation of premixed equilibrium chemistry has been completed for the OVERFLOW code, a chimera capable, complex geometry flow code widely used to predict transonic flowfields. The implementation builds on the computational efficiency and geometric generality of the solver.

Nomenclature

$\bar{\gamma}$	$\rho c^2/p$
ϵ	internal energy per unit mass ($\int_0^T c_v dT$)
ϵ_T	total internal energy per unit mass $\epsilon + \frac{1}{2}(u^2+v^2+w^2)$
$\tilde{\epsilon}$	internal energy per unit volume ($\int_0^T \rho c_v dT$)
κ	turbulent kinetic energy $\frac{1}{2}\sum \overline{u_i' u_i'}$
μ_T	turbulent eddy viscosity
ρ	mass per unit volume
θ	angle along sphere surface (degrees)
c	isentropic sound speed
h_T	stagnation enthalpy ($\epsilon + p/\rho + \frac{1}{2}(u^2+v^2+w^2)$)
L	reference length
p	static pressure
Q	conservative variables $[\rho, \rho u, \rho v, \rho w, \rho \epsilon_t]$
s	entropy
S_{ij}	Strain rate tensor $\frac{1}{2}\left(\frac{\partial u_i}{\partial x_j} + \frac{\partial u_j}{\partial x_i}\right)$
T	static temperature
u, v, w	cartesian velocity components
x, y, z	cartesian position coordinates

Introduction

Building on the successful application of the perfect gas version of OVERFLOW to hypersonic flowfields,[1] the next step in implementing finite rate chemistry capability in OVERFLOW is the generalization of the gas model from single species perfect gas to allow pressure and temperature as arbitrary functions of density and internal energy. The specific thermodynamic model used is that of Liu and Vinokur.[2] This model provides pressure and temperature for an equilibrium mixture of air over a wide temperature and pressure range.

Method

The Reynolds averaged Navier-Stokes equations, written in conservation law form are

$$\frac{\partial Q}{\partial t} + \frac{\partial F}{\partial x} + \frac{\partial G}{\partial y} + \frac{\partial H}{\partial z} = 0 \quad (1)$$

*Research Scientist, NASA Ames Research Center, Associate Fellow AIAA

†Research Scientist, NASA Ames Research Center

‡Senior Research Scientist, Eloret, Associate Fellow AIAA

§Research Scientist, ELORET, Member AIAA

Where

$$Q = [\rho, \rho u, \rho v, \rho w, \rho \epsilon] \quad (2)$$

$$F = \Big[\rho u, \rho u^2 + p + \tau_{xx}, \rho uv + \tau_{xy}, \rho uw + \tau_{xz}, \rho u(\epsilon_T + p + \tau_{xx}) + v\tau_{xy} + w\tau_{xz} + q_x\Big] \quad (3)$$

$$G = \Big[\rho v, \rho vu + \tau_{yx}, \rho v^2 + p + \tau_{yy}, \rho vw + \tau_{yz}, \rho v(\epsilon_T + p + \tau_{yy}) + w\tau_{yz} + u\tau_{yx} + q_y\Big] \quad (4)$$

$$H = \Big[\rho u, , \rho wu + \tau_{zx}, \rho wv + \tau_{zy}, \rho w^2 + p + \tau_{zz}, \rho w(\epsilon_T + p + \tau_{zz}) + u\tau_{zx} + v\tau_{zy} + q_z\Big] \quad (5)$$

where, we assume a simple Boussinesq type stress-strain relationship for the turbulence,

$$\tau_{ij} = 2(\mu + \mu_T)(S_{ij} - \frac{1}{3}S_{nn}) - \frac{2}{3}\rho\kappa\delta_{ij} \quad (6)$$

and the heat flux is given by the Fourier relation

$$q_i = (\frac{\mu}{P_r} + \frac{\mu_T}{Pr_t})\frac{\partial h}{\partial x_i} \quad (7)$$

The thermodynamic relation for pressure $p = p(\rho, \epsilon)$ is used in place of the perfect gas assumption ($p = \rho(\gamma-1)\epsilon$) in computing the fluxes of the momentum and energy equations, and the thermodynamic relation for temperature $T = T(\rho, \epsilon)$ enters into these equations indirectly, in the evaluation of molecular viscosity and thermal conductivity.

Implicit solution requires the calculation of Euler Jacobians ($\frac{\partial F_\epsilon}{\partial Q}$, $\frac{\partial G_\epsilon}{\partial Q}$, and $\frac{\partial H_\epsilon}{\partial Q}$) and for diagonalized methods, their eigenvectors and eigenvalues. The Euler fluxes are simply the Navier-Stokes fluxes with μ, μ_T, and k, set to zero. This generally involves an evaluation of the isentropic sound speed and derivatives of pressure with respect to ρ and $\rho\epsilon = \tilde{\epsilon}$. The sound speed is derived from the partial derivatives of the pressure returned by the thermodynamics module, and its current implementation allows a capability more general than mixtures of perfect gases in chemical equilibrium.

This solver is actually capable of predicting flows of any simple compressible substance where pressure and temperature are functions of only density and internal energy. The sound speed is given by the general relation for isentropic sound speed $c^2 = \left.\frac{\partial p}{\partial \rho}\right|_s$ As we have a table lookup routine which returns values of p, T, $\left.\frac{\partial p}{\partial \rho}\right|_\epsilon$ $\left.\frac{\partial p}{\partial \epsilon}\right|_\rho$ $\left.\frac{\partial T}{\partial \rho}\right|_\epsilon$ $\left.\frac{\partial T}{\partial \epsilon}\right|_\rho$, we need to be able to get the sound speed in terms of these variables and their derivatives.

From the Gibbs equation for a simple compressible substance,

$$ds = \frac{1}{T}(d\epsilon + pdv) = \frac{1}{T}\left(d\epsilon - pd\rho/\rho^2\right) \quad (8)$$

we get the relations

$$\left.\frac{\partial \epsilon}{\partial \rho}\right|_s = p/\rho^2$$
$$\left.\frac{\partial \epsilon}{\partial s}\right|_\rho = 1/T \quad (9)$$

which, along with the trivial relations

$$\left.\frac{\partial \rho}{\partial \rho}\right|_s = 1$$
$$\left.\frac{\partial \rho}{\partial s}\right|_\rho = 0 \quad (10)$$

allows us to transform the partial derivatives we have naturally as a result of the bicubic spline: $\left.\frac{\partial p}{\partial \rho}\right|_\epsilon$, $\left.\frac{\partial p}{\partial \epsilon}\right|_\rho$ into derivatives where $[\rho, s]$ are the independent variables. Thus we may calculate the sound speed from

$$c^2 = \left.\frac{\partial p}{\partial \rho}\right|_s = \left.\frac{\partial p}{\partial \rho}\right|_\epsilon + \left.\frac{\partial p}{\partial \epsilon}\right|_\rho \left.\frac{\partial \epsilon}{\partial \rho}\right|_s = \left.\frac{\partial p}{\partial \rho}\right|_\epsilon + \frac{p}{\rho^2}\left.\frac{\partial p}{\partial \epsilon}\right|_\rho \quad (11)$$

The derivatives of pressure required in the eigevector determination are

$$\chi = \left.\frac{\partial p}{\partial \rho}\right|_{\tilde{\epsilon}} = \left.\frac{\partial p}{\partial \rho}\right|_\epsilon - \frac{\epsilon}{\rho}\left.\frac{\partial p}{\partial \epsilon}\right|_\rho \quad (12)$$

$$\kappa = \left.\frac{\partial p}{\partial \tilde{\epsilon}}\right|_\rho = \frac{1}{\rho}\left.\frac{\partial p}{\partial \epsilon}\right|_\rho \quad (13)$$

(note the distinction between $\tilde{\epsilon}$, as opposed to ϵ).

Implementation

The base code used is OVERFLOW[3] which is a finite difference, chimera capable, complex geometry flow code widely used for perfect gas prediction. Matrix dissipation is used with central space differencing and multigrid to provide a rapid, robust solution method suitable for high speed flow with strong shock waves.[1]

OVERFLOW was modified to replace the perfect gas model built into the code with an arbitrary gas model, where the pressure and sound speeds are functions of the density and internal energy, as given in Liu.[2,4] An efficient table lookup method returns the pressure and temperature and their derivatives corresponding to a given value of $[\rho, \epsilon]$. A bicubic spline is used to produce smooth interpolations of both functions and their derivatives.

Four additional variables are added to the conservative variables $[\rho, \rho u, \rho v, \rho w, \rho \epsilon_t]$. The four additional field variables are $[p/p_\infty, \chi, Pr, T/T_\infty]$. These variables are obtained from the conservative variables at the start of each iteration, before the laminar viscosity is calculated. The perfect gas assumptions are then replaced by the use of the calculated pressures (in the momentum and energy fluxes, and their derivatives), temperatures (in the viscosity and conductivity calculations), and sound speed (in the implicit Jacobian calculations).

2nd-order central flux differencing combined with matrix dissipation[5,6] is used in forming the right hand side residuals, similar to the scheme used for perfect gas solutions.[1] The implicit solution method used is the Pulliam–Chaussee diagonal algorithm, with the eigensystem[7] the same as used to implement the matrix dissipation. Roe averaging is used in forming the matrices in the dissipation scheme. The pressure used to form the pressure switch function is that given by the $p = p(\rho, \epsilon)$, as opposed to the perfect gas assumption pressure.

The dissipation settings are similar to those suggested previously,[1] with the choices (unless otherwise noted) as

$$\begin{aligned} DIS_2 &= 4 \\ DIS_4 &= 0.2 \\ V_{\epsilon_l} &= 0.3 \\ V_{\epsilon_n} &= 0.3 \end{aligned} \tag{14}$$

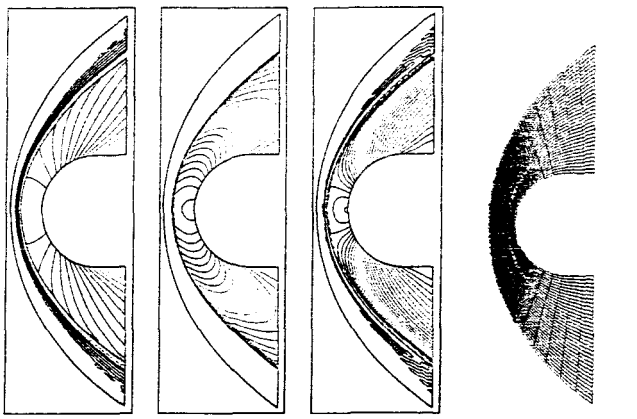

a) Pressure b) Temperature c) Density d) h_t on Grid

Fig. 1 $M_\infty = 32$, p = 10Pa = **Blunt Body Flowfield**

The settings for the initial (coarse grid) flow setup have modified eigenvalue limiters, ($V_{\epsilon_l} = V_{\epsilon_n} = 1.0$), which allows the shock to move off the body surface into the flowfield.

The multigrid method[6] has been modified to enhance the robustness of the method. The original multigrid method used a linear interpolation of the conservative variables to map the coarse grid solution onto the next finer grid. This interpolation is replaced with a linear interpolation of the variables $[\rho, u, v, w, \epsilon]$, which ensures a positive value of ϵ on the finer grid if ϵ is positive on the coarser grid.

Results

Inviscid Blunt Body Flow

This case is the inviscid flow past a blunt cylinder (Fig. 1) over a range of freestream static pressure and Mach number. The pressure conditions range from p = 1Pa (h=80km) to p = 10KPa(h=16km). The Mach numbers range from $M_\infty = 8$ (2.4km/sec) to $M_\infty = 32$ (9.5km/sec). The solutions were obtained on a 101 × 129 grid suitable for computation of a perfect gas, so much of the grid lies outside the shock.

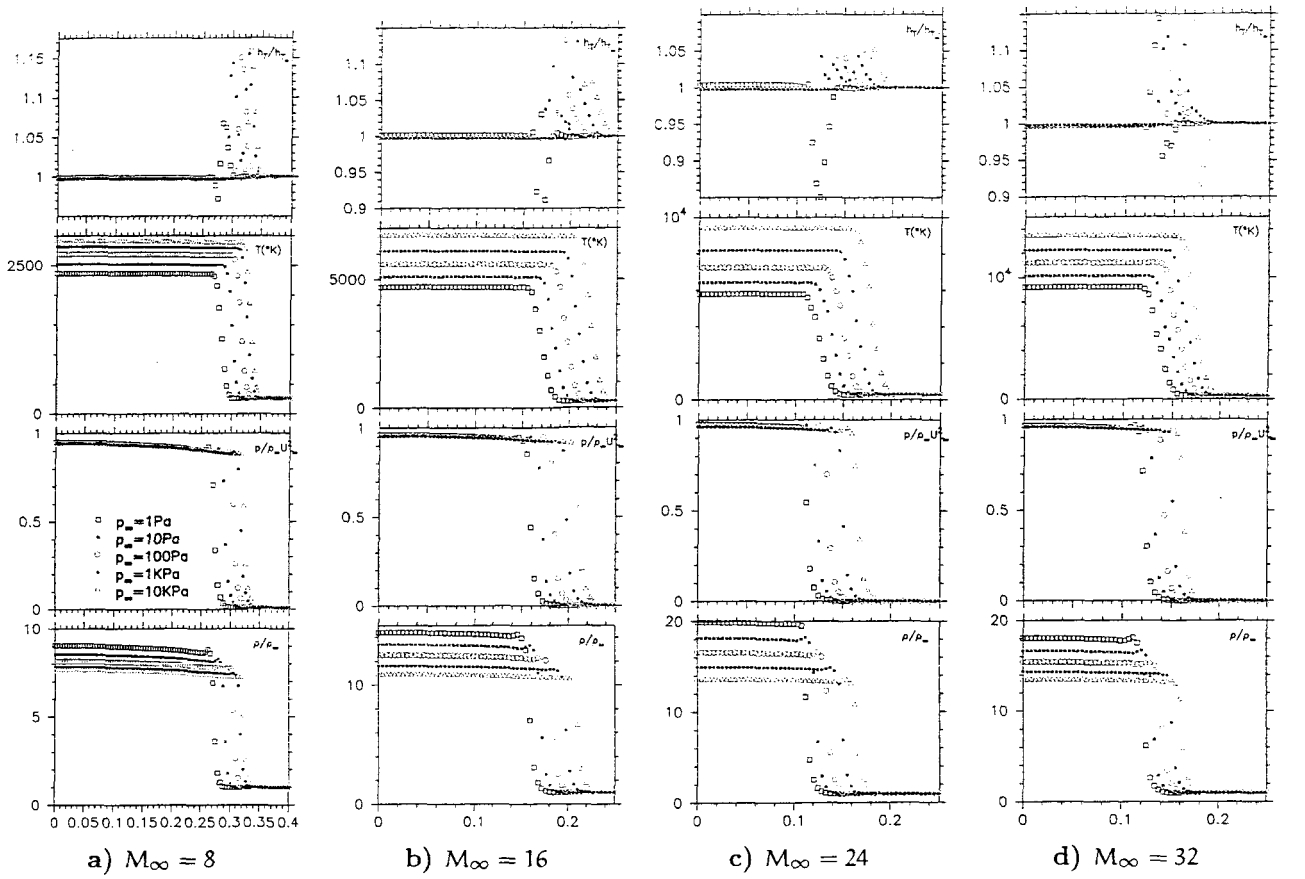

a) $M_\infty = 8$ b) $M_\infty = 16$ c) $M_\infty = 24$ d) $M_\infty = 32$

Fig. 3 Inviscid Cylinder Blunt Body Stagnation Line State

These solutions demonstrate the ability of the matrix dissipation to capture the shock over the wide range of conditions representative of earth atmospheric reentry. The smoothing parameters are unchanged over this entire range of conditions, and only the M = 32 cases required an adjustment of the CFL(halved from the other conditions) to obtain convergence (Fig. 2).

While all the cases show a similarity in the stagnation pressure profiles (Fig. 3), the variations of the temperature and density are more pronounced as the Mach number increases. At a fixed Mach number, a lower freestream pressure implies a lower post-shock temperature, as the dissociation is more complete at lower pressure. An interesting trend is evident in the density profiles. As the Mach number increase from 8 to 24, the post shock density increases, but from Mach 24 to Mach 32, there is a *decrease* in the post shock density especially at the higher pressures.

The preservation of total enthalpy across the shock is good at all Mach numbers. Along with being a check on the fidelity of the solution, this will be important in obtaining good heat transfer predictions in viscous flowfields. The pressure profiles in all cases are collapsed nicely when normalized by the Newtonian pressure, ρu_∞^2.

Laminar Flat Plate

The ability to correctly predict heat transfer and skin friction is as important as inviscid shock capturing capability. To check the viscous prediction capabilities, solutions for a laminar flat plat at freestream Mach numbers of 2 and 4 were obtained on 3 grids, 129×129, 65×65, and 33×33. The finest grid had a wall normal grid spacing of 2×10^{-6} (in units of plate length), and grid stretching factors less than 1.05. The coarser grids are obtained from the finer grid by bicimation (deleting every other point). Uniform inflow conditions are applied at the upstream and outer boundary. Simple extrapolation is used as the boundary condition at the outflow plane, and the constant temperature no slip is specified on the plate itself. A short region (12, 6 and 3 points respectively on the fine, medium and coarse grid) is specified as inviscid wall upstream of the plate.

The Reynold number of the flow (based on

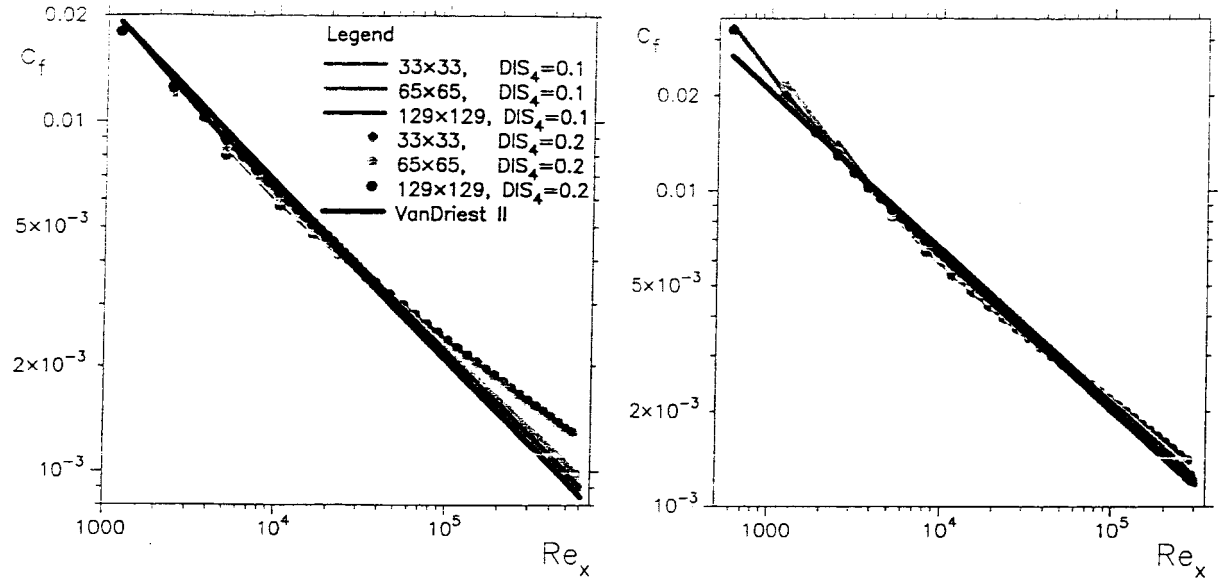

a) $M_\infty = 2$ b) $M_\infty = 4$

Fig. 4 Laminar Flat Plate Skin Friction Predictions

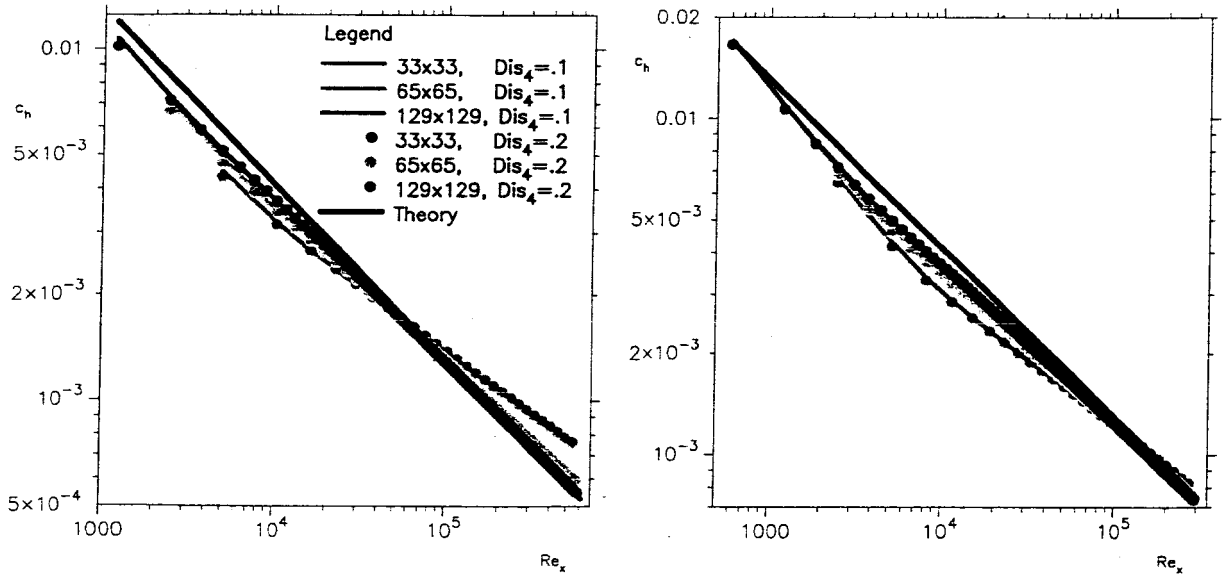

a) $M_\infty = 2$ b) $M_\infty = 4$

Fig. 5 Laminar Flat Plate Heat Transfer Predictions

plate length) is 600K for $M_\infty = 2$, and 300K for $M_\infty = 4$. The skin friction predictions are all nicely in agreement with theory (Fig. 4) and the heat transfer predictions (Fig. 5) are similarly good. These predictions are obtained with the same dissipation parameters used to produce the inviscid wedge and cylinder solutions. Also shown are the skin friction predictions with the lowered dissipation settings, which agree quite well with the 'standard' dissipation settings.

Turbulent Flat Plate

As turbulent flow is another area of interest for users of the code, a turbulent flat plate case was computed. This is a $M_\infty = 5$ case,[8] with an adiabatic wall. A special version of the gas properties table was created for this case, as the wall temperature is approximately 100°K lower when the actual variation of specific heat is used. The modified properties table had constant specific heats and Prandtl Number, with $\gamma = 1.4$ and $Pr = 0.73$, and Pr_t was chosen as 0.88, consistent

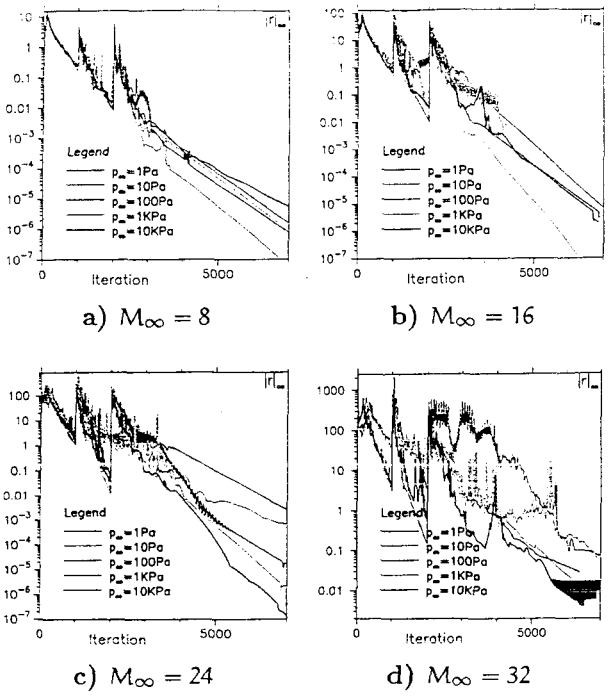

a) $M_\infty = 8$ b) $M_\infty = 16$

c) $M_\infty = 24$ d) $M_\infty = 32$

Fig. 2 Inviscid Cylinder Blunt Body Residual Histories

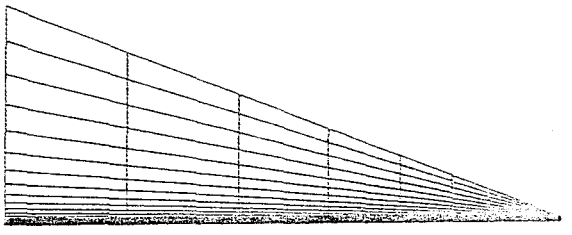

Fig. 6 Turbulent Flat Plate Grid(every 4th grid line shown)

with the earlier computations.[8] The Reynolds number based on plate length is as 140 Million, with a freestream static temperature of 273.15°K.

The solution is obtained on two grids, a fine grid of 129×257 (streamsize × wallnormal), and 65×129, the coarser grid as usual created from the finer by removing every other point. The grid is created by exponential stretching in both streamwise and wall normal directions with initial spacings of 10^{-4} and 10^{-6} of the plate length in each direction, respectively for the fine grid. The maximum stretching ratio of the the grid spacing is 1.05 streamwise and 1.04 wall normal. The outer boundary of the grid contains the weak shock created by nose of the flat plate. The grid wall normal spacing has $\Delta y_0^+ < 1$ for the coarser grid, with $\Delta y_0^+ < 0.1$ at the end of the fine grid.

A comparison of predictions using the Baldwin-Lomax(BL) algebraic model, the Spalart-Almaras[9](SA) one equation model, and the two equation Menter Shear Stress Transport[10](SST) are shown in Fig. 7. The SA implementation used is the published version, as opposed to the modified version standard in OVERFLOW. The skin friction predictions obtained are in good agreement with the Van Driest Theory, consistent with earlier work. Again, as with the laminar flat plate, solutions were obtained with the smoothing parameters halved, and the skin friction prediction predictions are again insensitive to the smoothing parameter choice(Fig. 8).

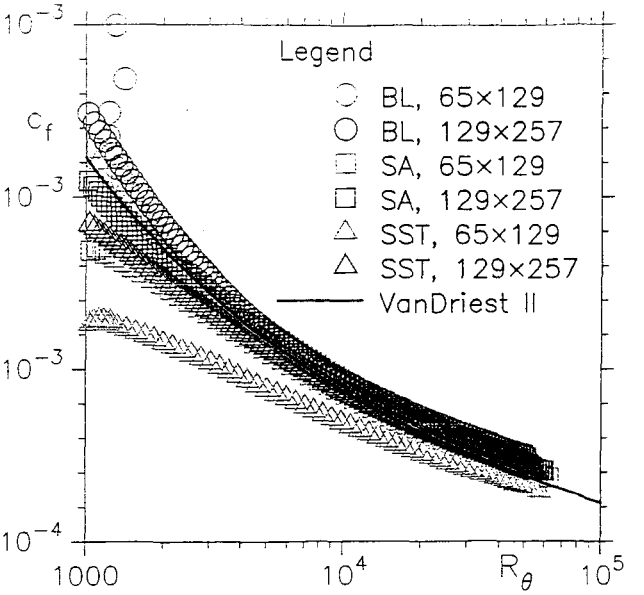

Fig. 7 Turbulent Flat Plate Skin Friction

Viscous Sphere

This case considers a laminar viscous flow over a 1m radius sphere at $M_\infty = 17.6$, p = 57.4Pa, $T_\infty = 200°K$, as shown in figure 9. This case is the benchmark case for LAURA, (http://hefss.larc.nasa.gov). The viscous wall boundary condition is no slip, $T_w = 500°K$. The finest grid used is 65(streamwise) by 129 (wall normal), with a constant wall grid spacing of 0.5μm. Two coarser grids were derived by this one by choosing every other point (33×65), and every fourth point(17×33). The solution is also obtained on a full 3D grid, with grid dimensions of $33 \times 65 \times 129$ (Streamwise×Circumferential×Wall Normal). The solution for the 3D grid lies on top of solution of the fine axisymmetric grid, and is both a check on the axisymmetric option and the

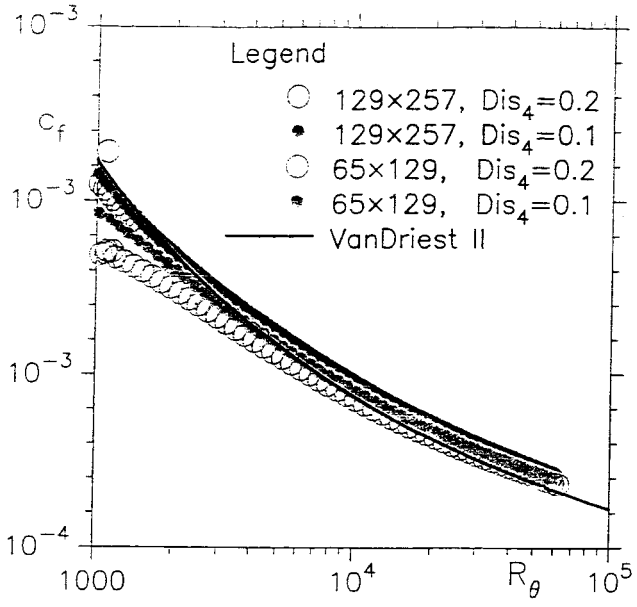

Fig. 8 Smoothing Parameters Sensitivity - SA Model

3D capability of the solver.

The stagnation profiles for this case (Fig. 10) are given in both external flow (linear in axial distance) and boundary layer(logarithmic in axial distance) coordinates. The pressure profile looks similiar to the inviscid case (Fig. 3), and agrees well with the prediction of LAURA, but here the stagnation enthalpy and static temperature variations are dominated by that of the boundary layer variations. The temperature predictions show the same boundary layer "lumpiness" predicted by LAURA, whereas the total enthalpy prediction is quite smooth over the same region. The 3D solution prediction is denoted by a dotted line in this figure, and follows the fine grid axisymmetric solution. Heat transfer predictions(Fig. 11) are similiar to those of the LAURA code.

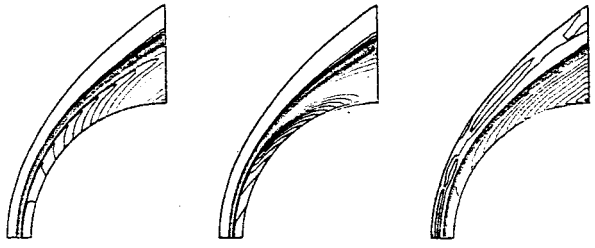

a) Pressure b) Temperature c) Density

Fig. 9 Viscous $M_\infty = 17.6$, p = 57.4Pa 1m Sphere

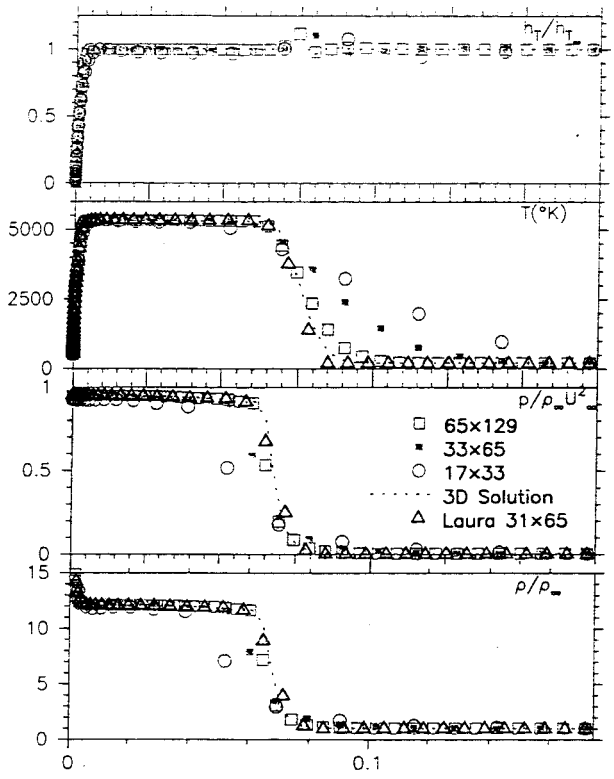

a) External Flow

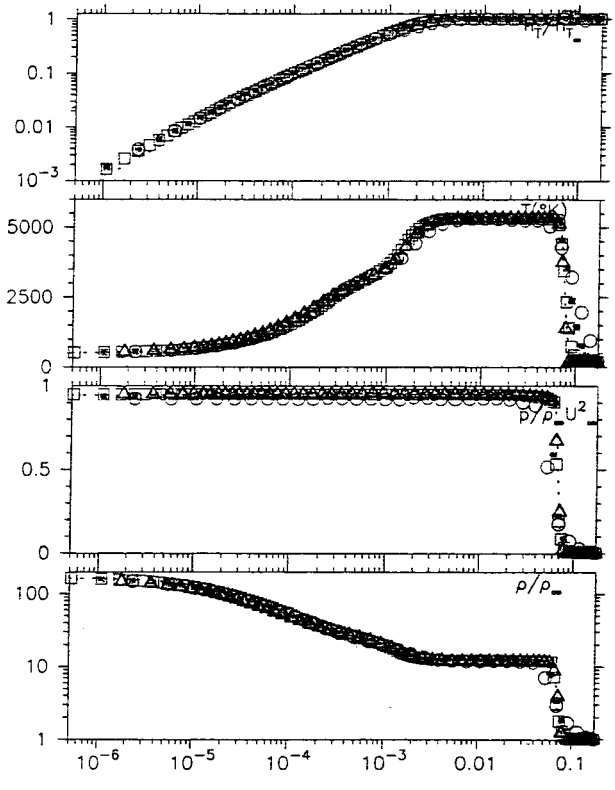

b) Boundary Layer

Fig. 10 Stagnation Streamline Profiles, $M_\infty = 17.6$, p = 57.4Pa 1m Sphere

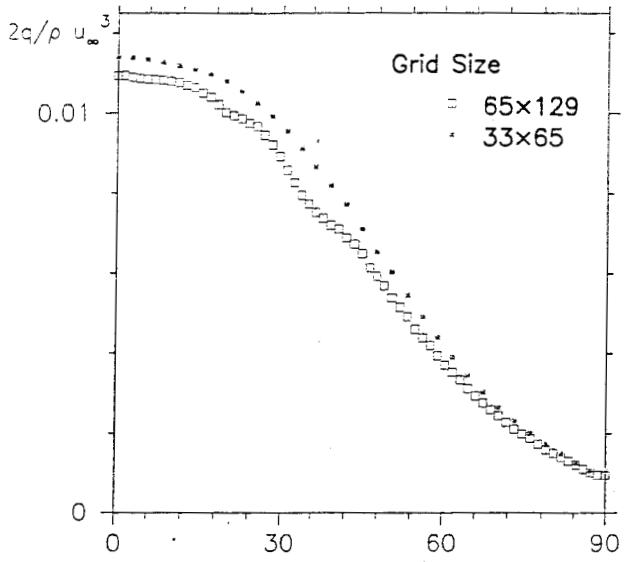

Fig. 11 Wall Heating Distribution, $M_\infty = 17.6$, p = 57.4Pa 1m Sphere

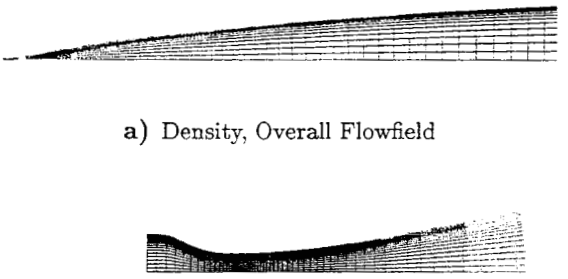

a) Density, Overall Flowfield

b) Reservoir Detail

Fig. 12 T10-97 (ONERA F4) Wind Tunnel Nozzle Flowfield

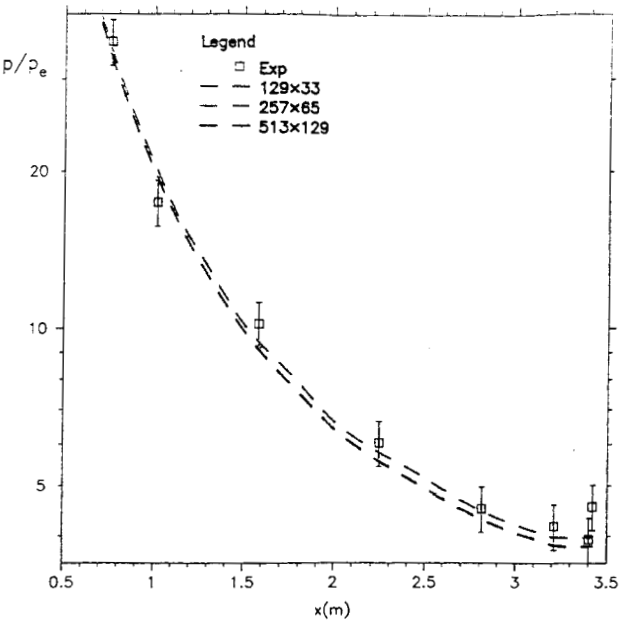

Fig. 13 Wall Pressure Distribution, T10-917 Test Case: Comparison with Experiment

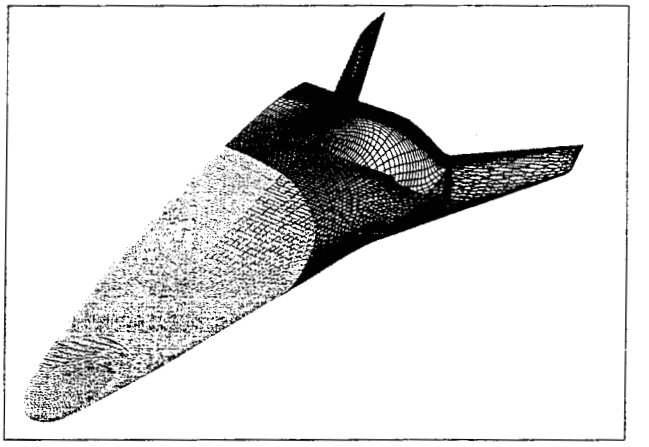

Fig. 14 X33 Surface Grid System

High Enthalpy Nozzle Expansion

This case highlights the ability to predict flowfields with extreme expansion. T10-97 is one of the First Europe–U.S. High Speed Flow Database test cases.[11] This case documents the flowfield in the ONERA F4 high enthalpy facility. The resevoir conditions are p = 373bar, $h_0 = 140T_\infty$, and the exhaust conditions are $T_\infty = 273°K$, $p_\infty = 68Pa$. The resevoir is charged with synthetic air, composed of $\frac{2}{9}O_2$ and $\frac{7}{9}N_2$ by mass fractions.

A sequence of three grids is again utilized, with the finest grid 513(Streamwise) × 129(WallNormal), and the coarser grids again created via 'bicimation'(removing every other point). The inflow plane is given p_t = constant, h_t = constant boundary conditions, the walls are no slip, fixed temperature ($T_w = 300°K$), and the outflow plane is 0 order extrapolation.

The solutions for this case depend critically on the air thermodynamic models,[11] and the current results (Fig. 13) are consistent with the results of other equilibrium air codes utilized to simulate this case. The predicted exit velocity is 4.68km/sec, consistent again with predictions by other equilibrium codes.[11]

X33

A final case is the X33, as solved in the previous perfect gas work.[1] This is a multiple zone case, at a freestream Mach number of 5.98, angle of attack of 40°, and Reynolds number of 3.3 Million. Wall temperature is constant at 300°K. The GASP and 'perfect gas' solutions are taken from that earlier paper, as is the grid system and

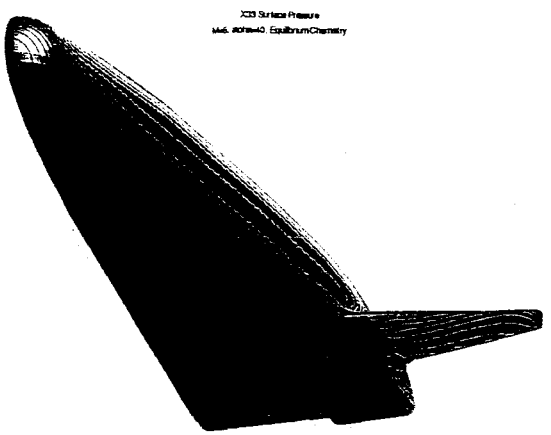

Fig. 15 Surface Pressure, X33

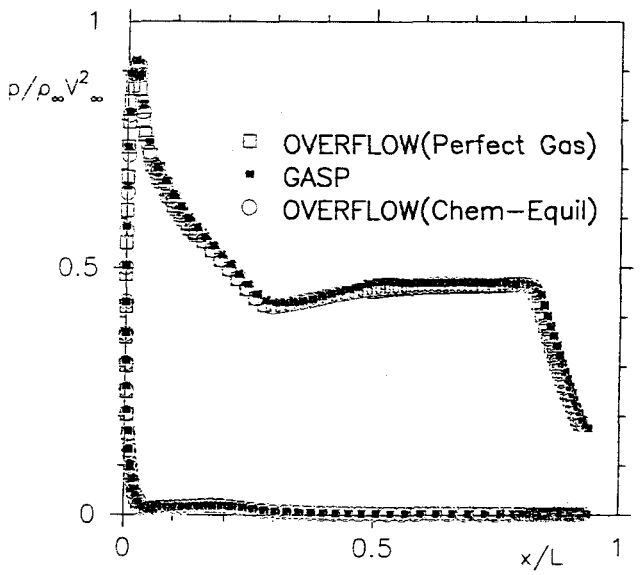

Fig. 16 Centerline Pressure Comparison

boundary conditions.

The surface pressure are in good agreement with the previous perfect gas and GASP solutions.[12] Surface heat transfer on the windward side of the vehicle is somewhat lower than that of the experiment,[13–15] where the perfect gas solution is higher. This is consistent with what one would expect from finite rate chemical reaction effects.

Discussion

The conclusions of the previous paper[1] for perfect gas cases continue to hold for the generalization of the thermodynamic model of overflow. Matrix dissipation yeilds predictions of similar quality as upwind MUSCL schemes, at much lower computational cost. Here the case can be

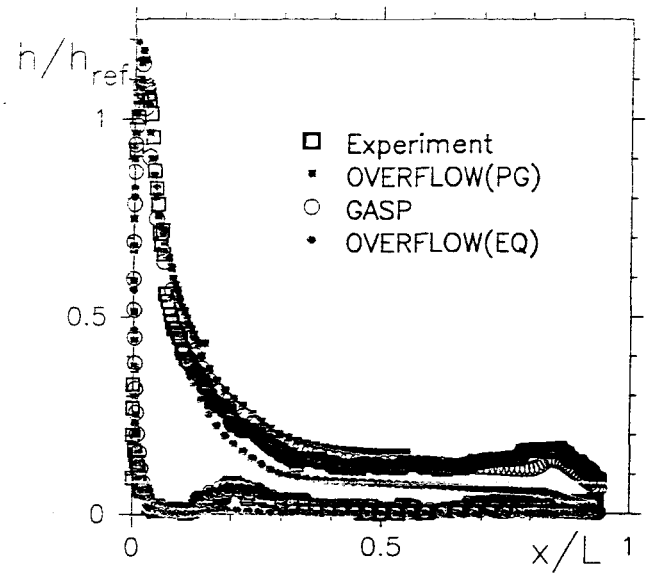

Fig. 17 Centerline Heat Transfer Comparison

made for Mach numbers up to 32, and over altitudes from sea level to 65km. A single set of parameters for the smoothing worked cases from inviscid cylinders to laminar and turbulent flat plates, as well as 3D geometries such as a sphere and the X33, and for extreme expansions such as the ONERA F-4 nozzle flow. The grids used were not "special" in any sense, and were constructed using standard tools (or re-using grids from other solvers), and the starting method worked reliably over all cases tried.

Multigrid had the same beneficial effect as seen in the perfect gas solutions, improving robustness, and accellerating convergence. Grid sequencing and multigrid work were utilized in every solution in this paper, and greatly aid the solution process.

Another piece of transonic technology which continued to work well with equilibrium chemistry is the Pulliam-Chausee diagonal algorithm. Although coupling this solution algorithm with chemistry is problematic, for solutions where the mean flow and chemistry systems can be solved in an uncoupled manner, this algorithm promises large computational cost savings.

The solution of the X33 system shows the feasibility of using the chimera system for high speed flowfields. The ability to use chimera to model complex geometries greatly facilitates the ability to obtain predictions for flight vehicles, and allows the tailoring of grid systems component by component. For rapid evaluation of an evolving system design, this capability is extremely important.

Conclusions

The present method shows promise for rapid prediction of complex flowfields where fully mixed chemical equilibrium is an appropriate approximation, and is another step in the overall goal of adding chemically reacting flow capability to OVERFLOW.

References

[1]Olsen, Michael E. and Dinesh K. Prabhu. "Application of OVERFLOW to Hypersonic Perfect Gas Flowfields". AIAA Paper 2001-2664, 2001.

[2]Liu, Yen and Vinokur, Marcel. "Equilibrium Gas Flow Computations. I. Accurate and Efficient Calculation of Equilibrium Gas Properties". AIAA Paper 89-1736, 1989.

[3]Buning, Pieter G. et al. Overflow user's manual. Version 1.8, NASA Ames Research Center, February 1998.

[4]Liu, Y. and M. Vinokur. "Equilibrium Gas Flow Computations. II. An analysis of Numerical Formulations of Conservation Laws". AIAA Paper 88-0127, Jan. 1988.

[5]Swanson, R. C. and Eli Turkel. "On Central-Difference and Upwind Schemes". *Journal of Computational Physics*, 101:292–306, 1992.

[6]Jespersen, D, Pulliam, T. H., and P.G. Buning. Recent enhancements to overflow. AIAA Paper 97-0664, January 1997.

[7]Liu, Yen and Marcel Vinokur. "Nonequilibrium Flow Computations. I. An Analysis of Numerical Formulations of Conservation Laws". *Journal of Computational Physics*, 83, No 2:373–396, August 1989.

[8]Bardina, J. E., Huang, P. G., and T.J. Coakley. "Turbulence Modeling Validation, Testing, and Development". NASA TM 110446, April 1997.

[9]Spalart, P.R. and S.R. Allmaras. "A one equation Turbulence Model for Aerodynamic Flows". *La Recherche Aerospatiale*, 1:5–21, 1994.

[10]Menter, F.R. "Two Equation Eddy Viscosity Model for Engineering Applications". *AIAA Journal*, 32:1299–1310, 1994.

[11]Sagnier, P. and Muylaert, M. "Synthesis of the Contributions to the Test Case T10-97 Wind Tunnel Nozzle". First Europe-US High Speed Flow Database Workshop-Part 2, November 12–14 2000, Naples, Italy, 1997.

[12]Prabhu, Dinesh K., Wright, Michael J., Marvin, Joseph G., Brown, James L., and Ethiraj Venkatapathy. "X-33 Aerothermal Design Environment Predictions: Verifiation and Validation". AIAA Paper 2000-2686, 34th AIAA Thermophysics Conference , June 19–22 2000, Denver CO, 2000.

[13]Merski, N. R. "Reduction and Analysis of Phosphor Thermography Data with the IHEAT Software Package". AIAA Paper 98-0712, 1998.

[14]Merski, N. R. "Global Aeroheating Wind-Tunnel Measurements Using Improved Two-Color Phosphor Thermography Method". AIAA Paper 98-0712, 1998.

[15]Hollis, B. R., Horvath, T. J., Berry, S.A, Hamilton, H.H., and S.J. Halter. "X-33 Computational Aeroheating Predictions and Comparisons with Experimental Data ". AIAA Paper 2000-2686, 34th AIAA Thermophysics Conference , June 19–22 2000, Denver CO, 2000.